INTERFACE

royalsocietypublishing.org/journal/rsif

Research

Cite this article: Zhang H-K, Zhou J, Fang W, Zhao H, Zhao Z-L, Chen X, Zhao H-P, Feng X-Q. 2022 Multi-functional topology optimization of *Victoria cruziana* veins. *J. R. Soc. Interface* **19**: 20220298.
https://doi.org/10.1098/rsif.2022.0298

Received: 16 April 2022
Accepted: 19 May 2022

Subject Category:
Life Sciences–Physics interface

Subject Areas:
biomechanics, biomimetics

Keywords:
Victoria cruziana, morphomechanics, vein network, topology optimization, rib-reinforced structures

Author for correspondence:
Xi-Qiao Feng
e-mail: fengxq@tsinghua.edu.cn

Electronic supplementary material is available online at https://doi.org/10.6084/m9.figshare.c.6016902.

Multi-functional topology optimization of *Victoria cruziana* veins

Hui-Kai Zhang[1], Jingyi Zhou[2], Wei Fang[1], Huichan Zhao[2], Zi-Long Zhao[3], Xindong Chen[1], Hong-Ping Zhao[1] and Xi-Qiao Feng[1,4]

[1]Department of Engineering Mechanics, AML, Institute of Biomechanics and Medical Engineering, Tsinghua University, Beijing 100084, People's Republic of China
[2]Department of Mechanical Engineering, Tsinghua University, Beijing 100084, People's Republic of China
[3]Institute of Solid Mechanics, School of Aeronautic Science and Engineering, Beihang University, Beijing 100191, People's Republic of China
[4]State Key Lab of Tribology, Tsinghua University, Beijing 100084, People's Republic of China

X-QF, 0000-0001-6894-7979

The growth and development of biological tissues and organs strongly depend on the requirements of their multiple functions. Plant veins yield efficient nutrient transport and withstand various external loads. *Victoria cruziana*, a tropical species of the Nymphaeaceae family of water lilies, has evolved a network of three-dimensional and rugged veins, which yields a superior load-bearing capacity. However, it remains elusive how biological and mechanical factors affect their unique vein layout. In this paper, we propose a multi-functional and large-scale topology optimization method to investigate the morphomechanics of *Victoria cruziana* veins, which optimizes both the structural stiffness and nutrient transport efficiency. Our results suggest that increasing the branching order of radial veins improves the efficiency of nutrient delivery, and the gradient variation of circumferential vein sizes significantly contributes to the stiffness of the leaf. In the present method, we also consider the optimization of the wall thickness and the maximum layout distance of circumferential veins. Furthermore, biomimetic leaves are fabricated by using the three-dimensional printing technique to verify our theoretical findings. This work not only gains insights into the morphomechanics of *Victoria cruziana* veins, but also helps the design of, for example, rib-reinforced shells, slabs and dome skeletons.

1. Introduction

Morphomechanics of biological tissues and organs has attracted much attention in recent years, with the aim to decode the interrelation of the geometric structures, chemical compositions, mechanical properties and biological functions of living systems. For instance, the elegant cellular architecture in plant tissues can effectively lower the stress magnitude in cell walls at the microscopic scale [1]. The active mechanical forces generated by their internal cells are crucial for the development of organoids and tissues at the macroscopic scale [2,3]. Recently, Yang *et al*. [4] studied the functions of highly porous bones of cuttlefishes and found that the functionally graded walls of the bones can enhance both their specific stiffness and energy absorption capacity. Fernandes *et al*. [5,6] reported that the double-diagonal and checkboard-like square morphology endows the skeleton of deep-sea glass sponges with outstanding strength robustness and buckling resistance.

Veins are widely observed in animal and plant tissues, and they usually possess a complex fractal topology. Veins can not only transport nutrients and promote the exchange of matters between different tissues, but also bear mechanical forces from the environment. The morphomechanics of veins is of significance for understanding the growth and development of biological tissues [7–11]. In plants such as *Victoria cruziana* (figure 1*a*,*b*), the vein networks can greatly improve the stiffness of leaves. Since its discovery in

THE ROYAL SOCIETY PUBLISHING

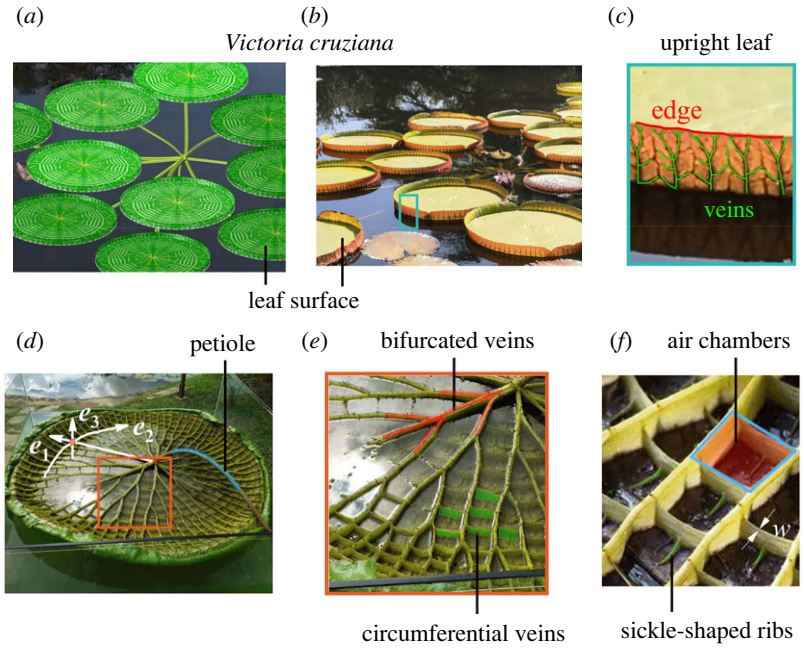

Figure 1. (*a*,*b*) Leaves of *Victoria cruziana*. (*c*) Bifurcated veins on an upright leaf. (*d*) The vein network on the bottom of the leaf with the radial direction $\boldsymbol{e}_1$ and the circumferential direction $\boldsymbol{e}_2$. The normal direction of the leaf is $\boldsymbol{e}_3$. (*e*) The bifurcated radial veins (red colours) and circumferential veins (green walls). (*f*) Magnified photo of the air chambers and sickle-shaped ribs, where *w* denotes the wall thickness of the circumferential veins. Photo (*b*) was taken at Beijing Botanical Garden, China, and photo (*d*) was taken at Yuanmingyuan Park, China.

1801 in the Amazon, *Victoria cruziana* has attracted extensive attention from both scientists and engineers [12–14]. It has the largest leaves among almost all aquatic plants, with a diameter of up to 3 m [15,16], rendering superior photosynthesis, such that it can survive in the tropical rainforest. Besides, *Victoria cruziana* leaves exhibit an excellent load-bearing capacity. A mature leaf could withstand a compressive force of up to 500 N [13]. *Victoria cruziana* veins have porous sponge microstructures, which form numerous air chambers at the bottom of the leaves and endow the leaves with a large buoyancy [13,14]. Though the biological functions of *Victoria cruziana* veins have been recognized, it remains unclear how their optimal topology is influenced by biomechanical factors.

The optimal design of free-form, rib-reinforced shell structures is of technologically significant interest in many engineering fields [17–23]. Attempts have been made to attain the optimized layout of ribs that can maximize the stiffness and strength of the structures [20,21,23–26]. In these previous studies, however, the functions of the ribs, such as heat conduction [27] and mass transport, have not been taken into account in the topological optimization of structures. The coupling effects of structural stiffness and nutrient transport on the layout of leaf veins were studied by using the theory of thin plates or shells [28–31]. To date, however, there is still a lack of an efficient topological optimization approach to investigate the three-dimensional hierarchical and multi-functional vein networks.

In this work, we investigate the three-dimensional and multi-functional vein network in *Victoria cruziana* leaves (figure 1*c*,*d*) by using a topology optimization method [32,33], in which both the mechanical performance and nutrient transport of veins are considered. This method can well reproduce the hierarchical vein networks in *Victoria cruziana* leaves, each of which has radial veins with gradient cross-sections and perpendicular to the leaf surface.

It is found that the vein network is optimal in the functions of both nutrient transport and load-bearing. Especially, the branching order, the non-uniform pressure, and component sizes of the network play important roles in the circumferential vein developments. Our findings also reveal that a better layout and morphology of the circumferential veins make a great contribution to the leaf stiffness, endowing the leaf with an excellent load-bearing capacity. In addition, artificial leaves fabricated by the Polyjet three-dimensional printing method [34] are used to verify our theoretical findings.

2. Material and methods

During the growth of a *Victoria cruziana* leaf, veins evolve on its lower surface to construct a network structure that can achieve its multiple biomechanical functions with high robustness [10,11]. Topology optimization [33,35–37] provides an efficient tool to design engineering structures with better properties and functions and to mimic the growth processes of biological structures. In the past few decades, some optimization techniques have been established, e.g. the model of solid isotropic material with penalization (SIMP) interpolation [33,36], the level set function [37], the moving morphable component [35] and the ground structure [38]. Optimization problems can be solved by using different approaches such as the optimality criteria (OC) method [33,36], the sequential linear/integer programming method [33,39], the method of moving asymptotes [40], and the non-gradient method [41–43]. These methods have been used in diverse fields of, for example, additive manufacturing [44,45], metamaterials [46–49], bionics [32,48,50,51], medical devices [52], flexible electronics [53], soft robotics [54,55] and aerospace [22,27,56].

In this work, the SIMP topology optimization method combined with the OC algorithm is applied to study the structural design of *Victoria cruziana* leaves. Particular attention is paid to the topological optimization of the veins on the lower surface of the leaf. The three-dimensional vein network, rather than the

leaf surface itself, is the design domain of optimization (figure 1). The mathematical programming of the compliance minimization problem is formulated as [32,33,36]

$$\begin{aligned} \min_{\mathbf{x}}:\ & J = \mathbf{F}^{\mathrm{T}}\boldsymbol{u} \\ \text{subject to:}\ & \mathbf{K}(\mathbf{x})\mathbf{u} = \mathbf{F}, \\ & V(\mathbf{x})/V_0 \le f^*, \\ & G(\mathbf{x}) \le R_{\max}, \\ & 0 \le x_i \le 1,\ (i = 1,2,\cdots,n), \end{aligned} \tag{2.1}$$

where the compliance J denotes the external work under a specified load, $\mathbf{u}$ and $\mathbf{F}$ are the global displacement and force vectors, respectively, $\mathbf{K}(\mathbf{x})$ is the global stiffness matrix, $\mathbf{x}$ (x_i, $i = 1, 2, \ldots, n$) is the vector of design variables, n is the total number of elements in the design domain, $V(\mathbf{x}) = \sum_{i\in\Omega} x_i v_i$ and $V_0 = \sum_{i\in\Omega} v_i$ are the material volume during the optimization process and the volume of the design domain, respectively; v_i is the volume of the ith element. $f = V(\mathbf{x})/V_0$ and f^* are the material volume fraction and the prescribed volume fraction. The geometric constraint $G(\mathbf{x})$ [50,57,58] could be added to equation (2.1) by tuning the maximum component size $R_{\max}$ for the local material layout in the optimization module of the software Abaqus. Assume that the veins and leaves are composed of the same material. The elastic modulus of element i can be described as

$$E(\rho_i) = E_{\min} + (E_{\mathrm{b}} - E_{\min})\rho_i^{\eta_1}, \rho_i \in [0, 1], \tag{2.2}$$

where E_{b} is Young's modulus of the material, $E_{\min} = 10^{-9}E_{\mathrm{b}}$ is a small Young's modulus assigned to the void regions to avoid numerical singularity [33,36], and η_1 is a penalty factor (typically, η_1 is about 3.0) introduced to obtain the black-and-white results. To accelerate the convergence, we take $\eta_1 = 4.0$ [32,59], which does not interfere with the objective value of optimization. Let $\rho_i (i = 1, 2, \ldots, n)$ denote the physical density of the ith element. To avoid the checkboard problem [33,36,60,61], we define

$$\rho_i = \frac{\sum_{j\in N_i} w(\boldsymbol{r}_i,\boldsymbol{r}_j)v_j x_j}{\sum_{j\in N_i} w(\boldsymbol{r}_i,\boldsymbol{r}_j)v_j}, \tag{2.3}$$

where $N_i = \{ j = |||\boldsymbol{r}_i - \boldsymbol{r}_j|| \le R \}$, and R is the filtering radius of the ith element. The elements located in this circle region all make contributions to the stiffness of the ith element. Besides, R may approximately control the minimal size of the optimized struts [33,36], $\boldsymbol{r}_i$ and $\boldsymbol{r}_j$ are the position vectors of element i and j ($j \in N_i$), respectively, $w(\boldsymbol{r}_i, \boldsymbol{r}_j) = \max(0, R - ||\boldsymbol{r}_i - \boldsymbol{r}_j||)$ is the weight factor, and v_j is the volume of element j ($j \in N_i$). For the minimum size control in topology optimization, the reader may refer to previous studies [57,62]. A smaller J indicates that the structure has a higher capacity to resist deformation under the specified load.

In this study, we also consider the efficiency of nutrient transport in the optimization of the vein network. The *Victoria cruziana* leaf has radial bifurcated or fractal veins similar to those in *Hedera canariens* leaf [63], as shown in figure 1*d*,*e*. Therefore, a two-dimensional model is used to analyse nutrient transport. The steady nutrient transport equation is written as [28,30,33,64,65]

$$\frac{\partial}{\partial x}\left(\kappa\frac{\partial \xi}{\partial x}\right) + \frac{\partial}{\partial y}\left(\kappa\frac{\partial \xi}{\partial y}\right) = -Q, \tag{2.4}$$

where ξ is the concentration of the nutrient matter, κ is the isotropic nutrient transport coefficient, and Q is the nutrient generating rate. The transport efficiency maximization problem [28,30,65] is expressed as

$$\begin{aligned} \min_{\mathbf{x}}:\ & C_{\mathrm{H}} = \boldsymbol{\xi}^{\mathrm{T}}\mathbf{K}_{\mathrm{H}}\boldsymbol{\xi} \\ \text{subject to:}\ & \mathbf{K}_{\mathrm{H}}(\mathbf{x})\boldsymbol{\xi} = \mathbf{F}_{\mathrm{H}}, \\ & V(\mathbf{x})/V_0 \le f^*, \\ & 0 \le x_i \le 1,\ (i = 1, 2, \ldots, n), \end{aligned} \tag{2.5}$$

where C_{H} is the objective function and denotes the generalized work driven by nutrient concentration ξ, $\mathbf{K}_{\mathrm{H}}$ is the global matrix of nutrients in the leaf (figure 1*a*,*b*), and $\boldsymbol{F}_{\mathrm{H}}$ is the vector of the nutrient transport from petiole (figure 1*d*). The nutrient transport coefficient κ in the ith element is [33,64]

$$\kappa(\rho_i) = \kappa_{\min} + (\kappa_{\mathrm{b}} - \kappa_{\min})\rho_i^{\eta_2}, \tag{2.6}$$

where κ_{b} denotes the normalized transport coefficient, $\kappa_{\min}$ is a small transport coefficient assigned to the void regions to avoid the numerical singularity [30], and η_2 is a penalty factor. In the following simulations, we set $\kappa_{\mathrm{b}} = 1.0$, $\kappa_{\min} = 10^{-4}\kappa_{\mathrm{b}}$, and $\eta_2 = 4.0$. The smaller the value of C_{H}, the more efficient the nutrient transport. To verify the effectiveness of this method, we provide two benchmark examples, with a square and a rectangular domain, respectively (electronic supplementary material, figure S1).

In this study, the optimization of the three-dimensional vein network is viewed as a synergetic process dictated by both its load-bearing capacity and nutrient transport efficiency, though many other factors may influence its growth. As observed in figure 1, the generation of the bifurcated veins in the radial direction $\boldsymbol{e}_1$ prominently promotes the nutrient transport efficiency [28,30,31]. The circumferential veins have a smaller wall thickness w than the radial veins (figure 1*f*). Therefore, it is emphasized that the circumferential veins in a *Victoria cruziana* leaf are optimized to sustain a balance of the nutrient transport efficiency and the overall stiffness of the leaf. Therefore, we divide the synergetic optimization process into two main steps. In §3.1, we first use the nutrient transport model to analyse the morphology of bifurcated veins in the radial direction, and in §3.2, we use the maximum stiffness model to elucidate the generation of circumferential veins.

3. Results

3.1. Radial veins

A *Victoria cruziana* leaf [12,13,18,66,67] has a circular and flat disc, surrounded by an upright leaf of several centimetres in height along the direction $\boldsymbol{e}_3$ (figure 1*c*,*d*). Complex and rugged veins are distributed on the lower surface of the disc (figure 1*d*), rather than embedded in the disc [8–11]. Along the radial direction $\boldsymbol{e}_1$ (figure 1*d*), the radial veins have hierarchical or fractal branches, with a decreasing height in the upward direction $\boldsymbol{e}_3$.

In the analysis of nutrient transport in a *Victoria cruziana* leaf, a nutrient resource is assumed at the centre (highlighted in red) of the circular design domain (figure 2 and electronic supplementary material, figure S2). The discretized design domain is composed of the uniform linear square 4-node elements with a dimensionless unit edge length (electronic supplementary material, figure S2). Using the method presented in §2, the optimized structures of radial bifurcated veins are generated by setting two key parameters, i.e. the target material volume fraction f^* and the filtering size R. For example, $R = 3$ denotes that the filtering radius is three times the uniform square mesh size. In figure 2*a*, as f^* increases, the branching order L (figure 2*b*) becomes larger and the value C_{H} becomes smaller, indicating a higher efficacy of nutrient transport. Besides, as the filtering radius R decreases and the branching order L increases, the sizes of the optimized veins decrease remarkably (figure 2*a*). This means that the structure containing a smaller branching order L features a lower capacity for nutrient transport (figure 2*c*,*d*), which motivates us to make a comparative analysis of the branching order in §3.2. Besides, the obtained bifurcated topology can

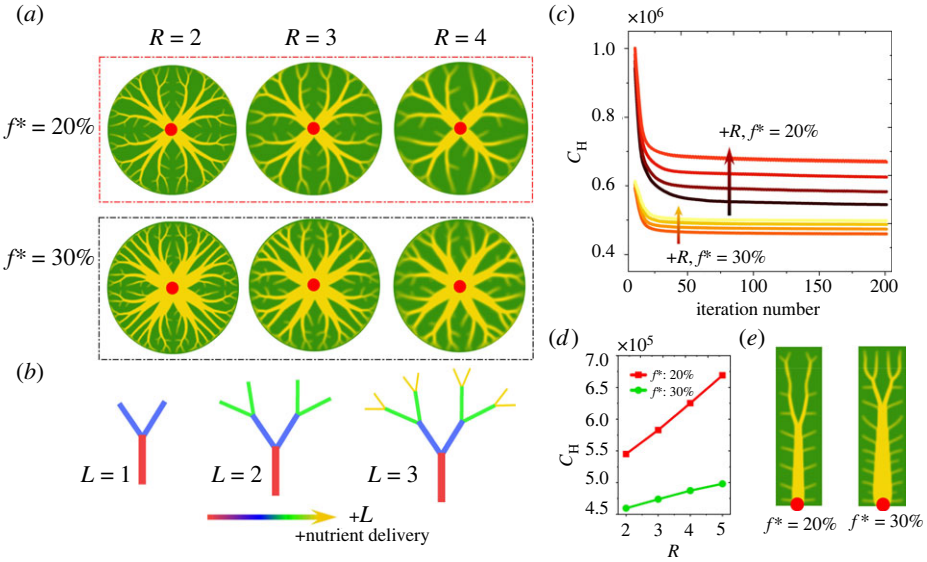

Figure 2. (*a*) Optimized and bifurcated veins for $f^* = 20\%$ and 30%, where we take different values of filtering radius R. (*b*) The nutrient delivery versus the branching order L. (*c*) Convergence of the objective function C_H. (*d*) Relation between the objective function C_H and the filtering radius R. (*e*) Veins in the upright leaves. The red, yellow, and green colours represent nutrient resources, optimized radial veins, and leaf, respectively.

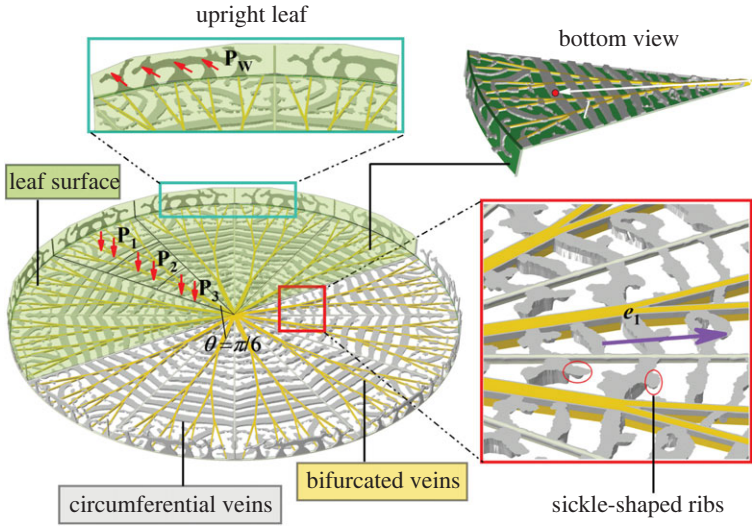

Figure 3. Numerical result of an optimized three-dimensional vein network, including the radial bifurcated veins (yellow colour) and optimized veins (grey colour). The veins consist of the circumferential structures, veins in the upright leaf, and the sickle-shaped ribs. The sickle-shaped ribs are along the radial direction (purple arrow). The pressures and wind load are $P_1 = P_2 = P_3 = 1.0 \times 10^{-7}$ MPa and $P_W = 1.0 \times 10^{-8}$ MPa, respectively, which are applied on the upper surface of the leaf (green colour region). The target volume fraction of material is $f^* = 30\%$, and the maximum size is $R_{max} = 4$ mm. The details of the design domain are given in electronic supplementary material, figure S4. *l* denotes the distance measured from the petiole to the marked red point. A larger *l* indicates a wider layout of the optimized circumferential veins.

transport nutrients efficiently from the radial veins to the external edges (figure 1*e*) of the upright leaf.

3.2. Circumferential veins

The superior load-bearing capacity of a mature *Victoria cruziana* leaf originates from numerous air chambers enclosed by the radial and circumferential veins. These air chambers (figure 1*f*) endow the leaf with astonishing buoyancy [13,18,68]. Besides, the plate-like veins in the circumferential direction (figure 1*e*,*f*) connect the radial veins. The circumferential and radial veins work synergistically as a network to stiffen the leaf structure. Here, instead of considering the maximal buoyancy as the objective of optimization [60,69,70], we apply mechanical pressures and wind loads on the leaf surface (figures 1*a*,*b* and 3, and electronic supplementary material, figure S3) to mimic the natural environment of *Victoria cruziana* leaves.

In §3.1, we have studied the influence of the branching order L on the nutrient transport efficiency, and now we further address its influence on the load-bearing capacity. For illustration, we compare the parametrized and bifurcated vein networks with $L = 3$ and $L = 2$ (electronic supplementary material, figure S3, and figure 2*b*). In the first example, we consider a radial vein with $L = 3$, as shown in electronic supplementary material, figure S4. The three-dimensional

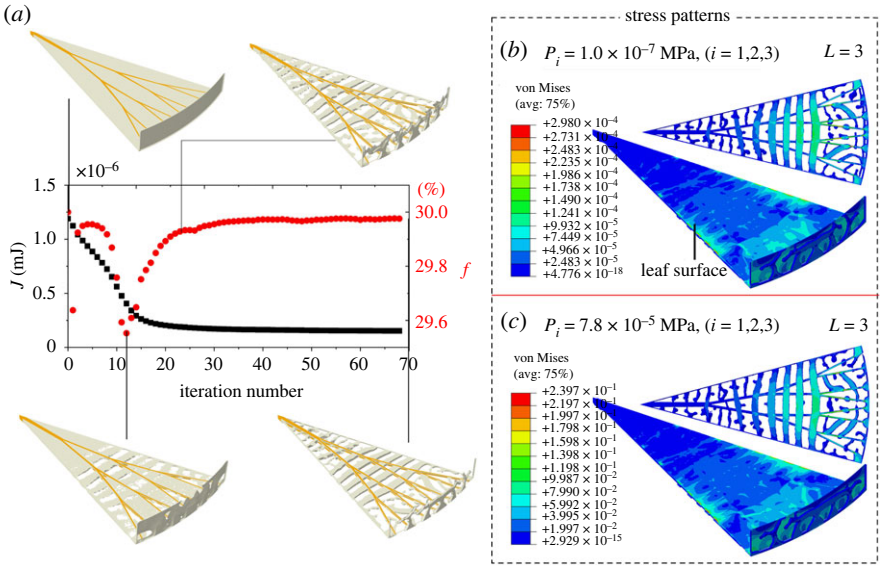

Figure 4. Iteration history and stress analysis. (*a*) History of the objective function J and the volume fraction f of material. The yellow and grey colours are the bifurcated veins and the design domain for the circumferential veins, while the leaf surface (green colour in figure 3) is hidden for clear illustration of the optimized veins. (*b*,*c*) The von Mises stress fields under uniform pressures of 1.0×10^{-7} MPa and 7.8×10^{-5} MPa, respectively, showing that the pressure amplitude has little influence on the optimization results of the vein topologies and stress patterns. The corresponding objective function values are $J = 1.55 \times 10^{-7}$ mJ and $J = 0.096$ mJ, respectively.

optimization model consists of three parts, including the leaf with a small thickness (green region, electronic supplementary material, figure S4a), the radial vein (yellow region, electronic supplementary material, figure S4b), and the pre-designed domain for optimizing the circumferential veins (grey regions, electronic supplementary material, figure S4b). All geometric parameters are shown in electronic supplementary material, figure S4c, where the thickness decreases from $t_1^{(d)} = 2.0$ mm to $t_2^{(d)} = 0.6$ mm along the radial direction $\boldsymbol{e}_1$. The radius and thickness of the leaf are $r = 100.0$ mm and $t^{(s)} = 1.0$ mm, respectively. The height of the upright leaf is set as $h = 9.6$ mm. To reduce the computational cost, we analyse only one representative part of the sector domain (electronic supplementary material, figure S4a), with a central angle of $\theta = \pi/6$, as shown in figure 3 and electronic supplementary material, figure S4a.

The applied pressure is uniformly distributed on the three regions of the upper leaf surface (figure 3) with $\mathbf{P}_1 = \mathbf{P}_2 = \mathbf{P}_3$, and the uniform wind load $\mathbf{P}_w$ is normally applied on the surface of the upright leaf (figure 3 and electronic supplementary material, figure S4a). The loads keep constant during the optimization process. In the stiffness maximization problem, the Young's modulus and Poisson's ratio of the basal material are taken as $E_b = 10$ MPa and $\nu = 0.3$, respectively [12].

The model (electronic supplementary material, figure S4a) is discretized into 0.31 million 8-node linear brick, reduced integration elements (C3D8R), and the maximum element size is 0.2 mm (electronic supplementary material, figure S4d). This large-scale optimization problem [32,51] is performed by the commercial software Abaqus, where we make use of its parallel computation platform. The optimization problem is solved by the OC algorithm [33,36]. The target volume fraction f^* of material is set as 20% or 30% in different cases. By changing the maximum geometric size R_{max} defined in equation (2.1), the local accumulation of material can be avoided [50,57,58].

It was reported that a *Victoria cruziana* leaf with a diameter of 3 m can bear a load of about 500 N (https://www.52zzl.com/wanglian/4181.html), which induces a pressure of 7.07×10^{-5} MPa. This value is close to our experimental test result of 6.4×10^{-5} MPa, which will be described in §4. It is worth mentioning that due to the small thickness of the leaf, a larger pressure may cause distortions of the three-dimensional elements, which may cause an unexpected stop of iteration (electronic supplementary material, figure S4d). To overcome this difficulty, we specify the pressure on the leaf surface with a smaller value $P_1 = P_2 = P_3 = 1.0 \times 10^{-7}$ MPa in figure 3, and the hypothetical wind load $P_W = 1.0 \times 10^{-8}$ MPa. Linear elastic finite-element analysis is made in the optimization process. The leaf edges (electronic supplementary material, figure S4a) and all freedoms in the Euclidean space of the petiole are fixed. In the design domain, the target volume fraction of material is set as $f^* = 30\%$.

Figure 3 shows the optimized structure with $J = 1.55 \times 10^{-7}$ mJ, which features a complex three-dimensional vein network. Its circumferential structures connect the bifurcated veins. This kind of layout not only promotes the transport of nutrients but also more importantly enhances the stiffness of the whole leaf. Numerous air chambers separated by the veins (figure 3) endow the leaf with an outstanding buoyancy. It is seen that the distribution of the circumferential veins is approximately isometric along the radial direction $\boldsymbol{e}_1$. However, due to the coupled effects of wind loads and pressures, the veins near the edge evolve complex morphologies (figure 3).

In addition, there are many auxiliary ribs along the radial direction $\boldsymbol{e}_1$ (figure 3), which can increase the flexural stiffness of the circumferential veins. As shown in figure 1*f*, due to the gradient thickness of the veins in the direction $\boldsymbol{e}_3$, a big pressure difference could be generated by the captured air between the adjacent air chambers (figure 1*f*). This helps understand why the *Victoria cruziana* leaf evolves these kinds of ribs to support the circumferential veins.

The history of the objective function J and the volume fraction f of the material (figure 4*a*) show that the optimization algorithm is effective and stable. A lower stress is uniformly distributed over the middle part of the leaf surface (figure 4*b*), while higher stress concentration occurs on the leaf edges because of the boundary condition. Besides, a high-tension stress field occurs on the circumferential veins

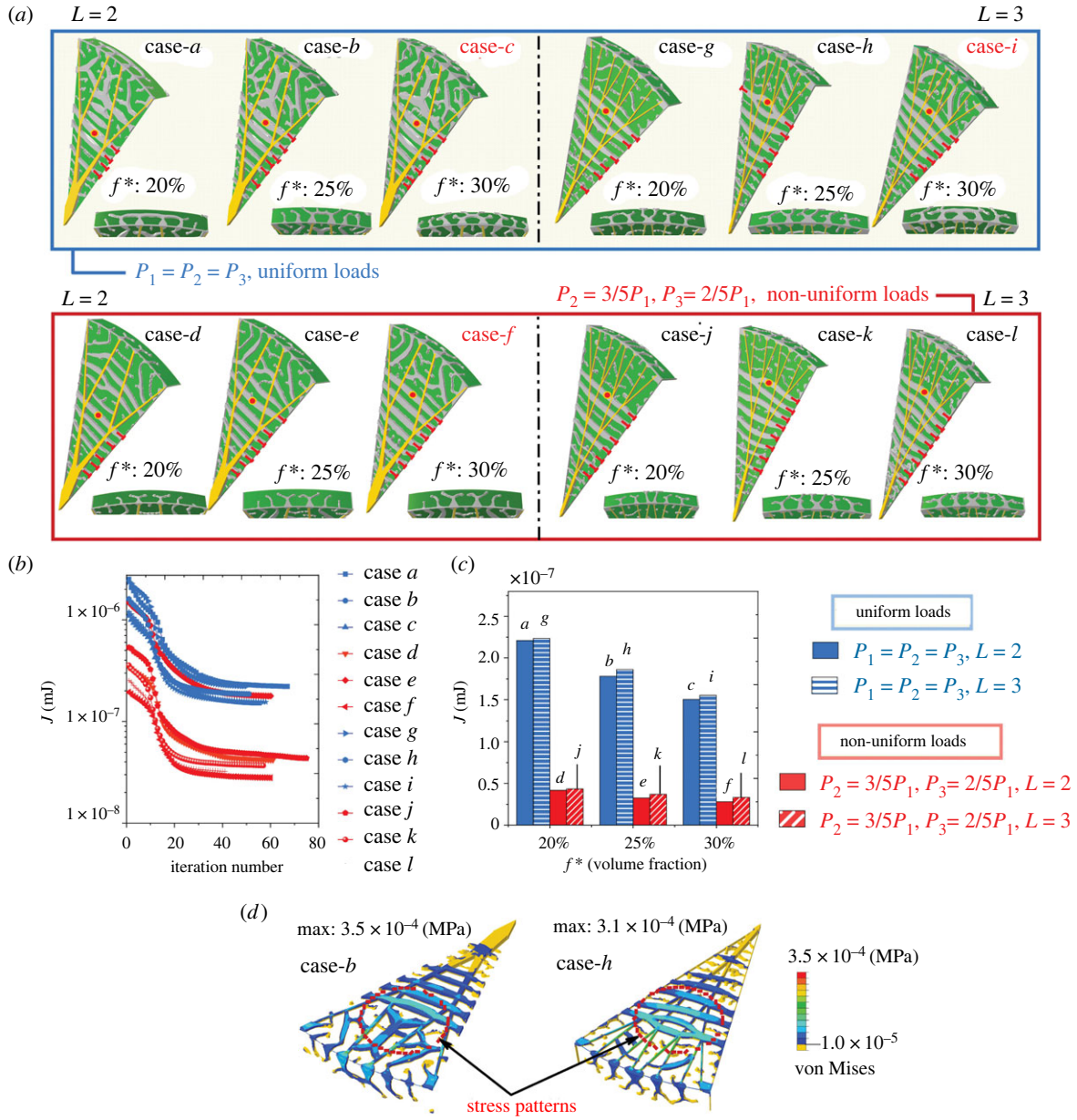

Figure 5. Optimization results under different values of L and pressure. (*a*) Optimized veins in the 12 cases, which are divided into four groups. (*b*,*c*) The iteration histories of J in all cases. Under a specified value of f^*, the stiffness of the optimized structure with $L = 3$ has a slight difference from that with $L = 2$. (*d*) Stress distributions in cases *b* and *h*. It is seen that increasing the branching order can make the stress distribution in the veins more uniform and thus enhance the load-bearing capacity of the leaf.

(figure 4*b*), suggesting that the compressive force applied on the leaf surface induces the tensile deformation of the circumferential veins. This deformation mechanism ensures the superior load-bearing capability of the *Victoria cruziana* leaves. Further, we simulate two more cases, which undergo higher pressures of 6.4×10^{-5} MPa (electronic supplementary material, figure S5) and 7.8×10^{-5} MPa (figure 4*c*), respectively. The stress fields show a similar pattern, as shown in figure 4*b*. In the following analysis, therefore, we will assume a smaller pressure of 1.0×10^{-7} MPa to study the design of circumferential veins.

3.3. Effects of branching order and non-uniform pressure

Now we investigate the effects of the branching order of radial veins on the structural stiffness of the *Victoria cruziana* leaf. As concluded in §3.1, under a fixed material dosage, a vein network with a smaller L yields a lower nutrient delivery.

Further, we examine the effect of non-uniform pressure on the optimized architecture of veins. Figure 5 shows the optimization results of 12 representative examples under different pressures and branching orders. In these examples, we take the same optimization conditions, with the maximum component thickness $R_{max} = 4$ mm, the wind load $P_W = 1.0 \times 10^{-8}$ MPa and the element size being 0.2 mm. These examples are classified into the following four groups:

(1) *Group I*: This group contains the cases *a*–*c*, which have a uniform pressure $P_1 = P_2 = P_3 = 1.0 \times 10^{-7}$ MPa and bifurcated radial veins with $L = 2$.
(2) *Group II*: This group, including cases *d*–*f*, have radial veins with $L = 2$ and a hypothetic gradient pressure with $P_2 = 3/5P_1$, $P_3 = 2/5P_1$ and $P_1 = 1.0 \times 10^{-7}$ MPa.

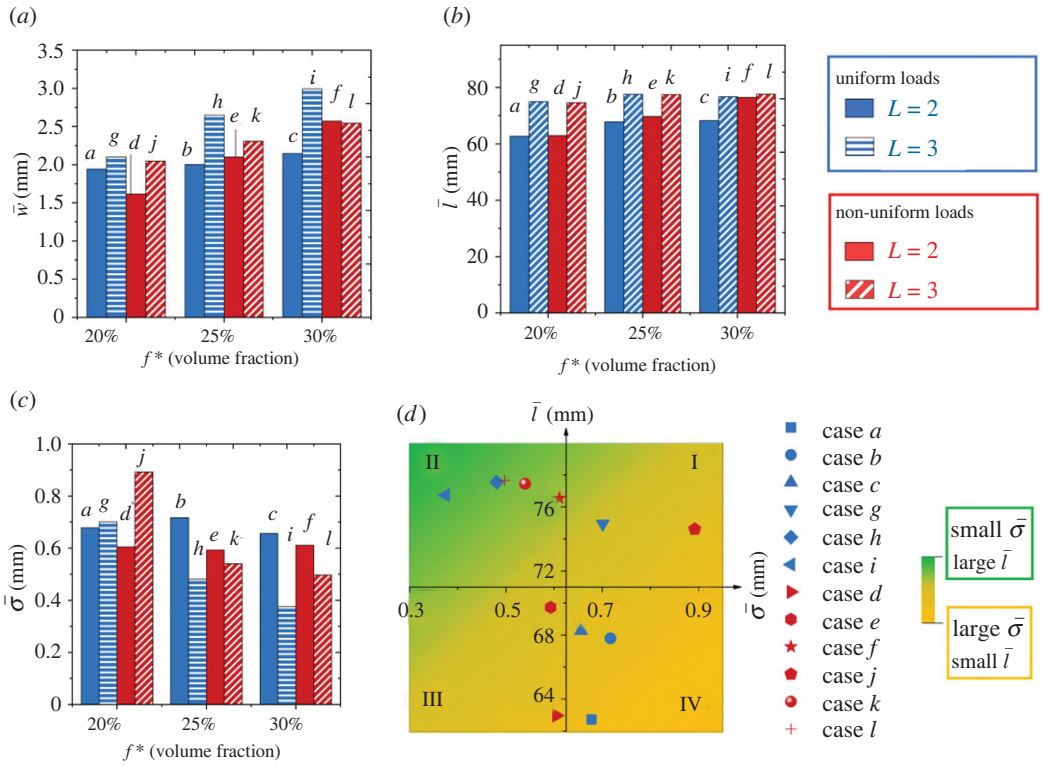

Figure 6. (*a*) The average wall thickness $\bar{w}$ of the circumferential veins. (*b*) The maximum layout distance $\bar{l}$ from the red point to the petiole (figure 5*a*). (*c*) The uniform standard error $\bar{\sigma}$ of the wall thicknesses of the circumferential veins along the direction $\boldsymbol{e}_1$. (*d*) The phase diagram in the $\bar{l}$–$\bar{\sigma}$ space. Quadrants I and IV indicate the optimized veins with non-uniform wall thickness. The optimized structures in quadrant III have a smaller layout distance. In region II, the circumferential veins have a relatively more uniform wall thickness and larger layout.

(3) *Group III*: This group (cases *g*–*i*) has the branching order $L = 3$, and the same uniform pressure as that in group I.
(4) *Group IV*: In this group (cases *j*–*l*), the branching order is $L = 3$, and the pressure is the same as that in group II.

Besides, the three cases in each group have the target volume fractions $f^* = 20\%$, 25% and 30%, respectively.

As can be seen from the simulation results in figure 5*b*, the histories of the objective function J in these examples decrease smoothly in the logarithmic coordinate system. Figure 5*c* reveals that a higher material usage will enhance the stiffness of the leaf and converge to a smaller value of J. It is also seen from figure 5*c* that, under a specified value of f^*, the stiffness of the optimized structure with $L = 3$ has a slight difference from that with $L = 2$. For example, the optimized J of cases *a* and *g* are 2.21×10^{-7} mJ and 2.24×10^{-7} mJ, respectively. However, increasing the branching order can make the stress distribution in the veins more uniform, thus enhancing its load-bearing capacity (figure 5*d*).

Now we compare the values of the parameters w, l and σ in the 12 cases, which quantify the morphological features of the circumferential vein networks. Here, $\sigma = \sqrt{\sum_i^n (w_i - \tilde{w})^2/N}$ defines the standard error of the wall thicknesses w_i of the circumferential veins, where N is the counted number of the circumferential veins, which are highlighted with red symbols in figure 5*a*, and $\tilde{w} = \sum_i^N (w_i)/N$ is the averaged value of w_i (more details are given in electronic supplementary material, tables S1–S5). A small σ indicates that the wall thicknesses of the circumferential veins at different radial positions are close to each other. Due to the thickness variations of the veins, we measure twice to obtain the average values of these parameters, denoted as $\bar{w} = (\tilde{w}_1 + \tilde{w}_2)/2$, $\bar{l}$ and $\bar{\sigma}$.

Figure 6 gives the statistical average wall thickness $\bar{w}$, the maximum layout distance $\bar{l}$, and the standard error $\bar{\sigma}$ in all 12 cases (figure 5*a*). In figure 6*a*, it is found that a larger branching order L promotes a larger $\bar{w}$ under the same material dosage. For example, the radial veins with $L = 2$ are thicker than those with $L = 3$, as shown in figure 5*a* (cases *a* and *g*), which both have $f^* = 20\%$. Therefore, the optimized leaf in case *g* needs a larger $\bar{w}$ for the circumferential veins to compensate for the loss of its stiffness compared to case *a*. This finding is also verified by the cases under non-uniform pressures (e.g. cases *d* and *j*).

In addition, the result in figure 6*b* reveals that the maximum circumferential vein layout distance $\bar{l}$ has a remarkable increase in the case with a larger L. This finding can also be observed in the vein network of *Victoria cruziana* (figure 1), where its circumferential veins extend to the leaf edge.

As shown in figure 6*c*, the vein networks with a larger branching order have a smaller $\bar{\sigma}$. This tendency becomes more obvious as the material volume increases. When a non-uniform pressure is also applied to the leaf, $\bar{\sigma}$ is considerably reduced for the veins with a branching order of $L = 2$.

To further investigate the combined effects of the branching order and non-uniform pressure on the optimal morphology of circumferential veins, we give the $\bar{l}$ versus $\bar{\sigma}$ relations for all the 12 cases in figure 6*d*. The coordinate origin is set at the centre of $\bar{l}$–$\bar{\sigma}$, and the examples in quadrant II have a similar vein morphology and nutrient delivery capacity to the real veins of *Victoria cruziana*. The highlighted points in this region, including cases *h*, *i*, *k* and *l*, have a lower $\bar{\sigma}$ and a higher $\bar{l}$, because of the contributions of the larger branching order $L = 3$ and

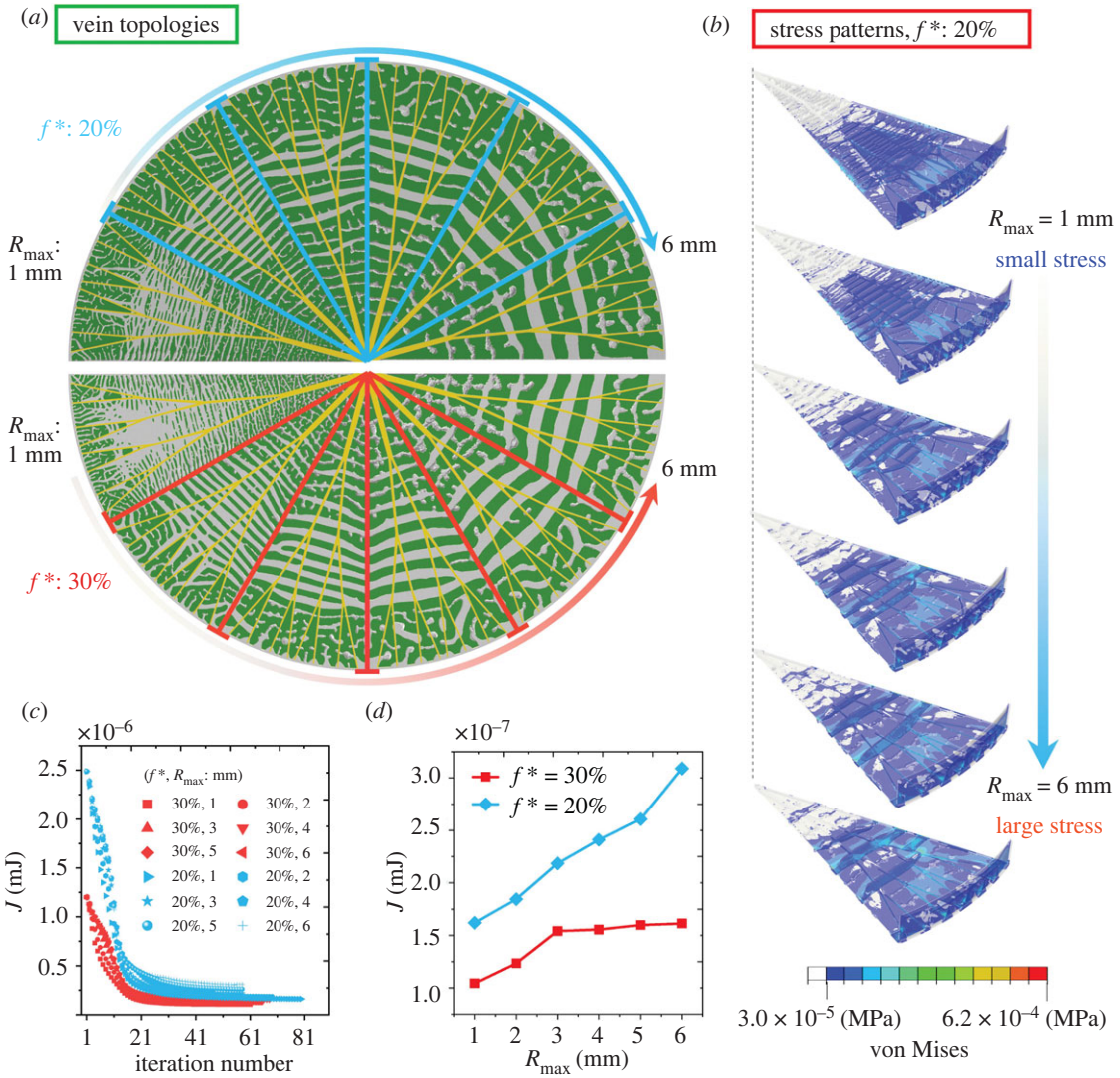

Figure 7. Effects of R_{max} on the leaf stiffness and vein morphologies. (*a*) Optimized leaves of all cases. (*b*) Stress patterns with respect to R_{max}. (*c*,*d*) Histories of the objective function J with R_{max}. It is found that with increasing R_{max}, the maximal stress in the veins increases with R_{max} while the leaf stiffness decreases.

non-uniform pressure. By contrast, the radial veins of $L = 2$ have a larger $\bar{\sigma}$ and a smaller $\bar{l}$ in quadrant IV.

3.4. Size and morphology variations of circumferential veins

In the simulations, we set the maximal component thickness R_{max} in order to avoid material build-up in the circumferential veins during optimization. For example, $R_{max} = 3.0$ mm means that the wall thicknesses w of all circumferential veins are limited to be smaller than 3.0 mm (electronic supplementary material, tables S6–10). In this section, a finer grid is used to discretize the three-dimensional design domain, where the largest element size is 0.14 mm, with a total of 0.57 million three-dimensional elements. We take cases *g* and *i* (figure 5*a*) to uncover the effect of R_{max} on the leaf stiffness and vein morphology, with the target volume fraction of 20% and 30%, respectively (figure 7*a*). The two examples have a radial vein with $L = 3$ (electronic supplementary material, figure S3b). For each case, the value R_{max} ranges from 1 mm to 6 mm (figures 7*a* and 8*a*). Similarly, as discussed in §3.3, the parameters $\bar{l}$, $\bar{w}$ and $\bar{\sigma}$ are all calculated to examine the structural variations as shown in figure 8 with respect to R_{max} (electronic supplementary material, tables S6 and S10).

In figure 8*b*, the average wall thickness $\bar{w}$ increases with respect to R_{max}, which leads to a decrease in the number of circumferential veins N (figures 7*b* and 8*c*). Thus, the stress in the optimized veins gradually increases (figure 7*b*), resulting in a decrease in the leaf stiffness with increasing R_{max} (figure 7*c*,*d*).

In figure 8*d*,*e*, with increasing R_{max}, $\bar{l}$ decreases but $\bar{\sigma}$ increases. In the phase diagram of $\bar{l}$–$\bar{\sigma}$ (figure 8*f*), three highlighted points are located in the upper-left region, where the vein networks can yield a high stiffness and load-bearing capacity of the leaf. By contrast, one example is located at the left-bottom corner, which has smaller $\bar{l}$ and N, indicating a poor vein topology in the leaf. The size R_{max} plays a signficant role in the optimization of the vein net work and the mechanical behaviour of the leaf.

4. Experiments

To qualitatively verify the optimization results (figure 5*a*), we fabricate biomimetic leaves by using the Polyjet three-dimensional printing technique [34]. Three samples (I, II and III) are made, as shown in figure 9*b*, corresponding to the cases *c*, *f* and *i* (figures 5*a* and 9*a*), respectively. The minimum printing size of Objet 30 prime made by Stratasys is 16 µm, and the printing and supporting materials are polypropylene

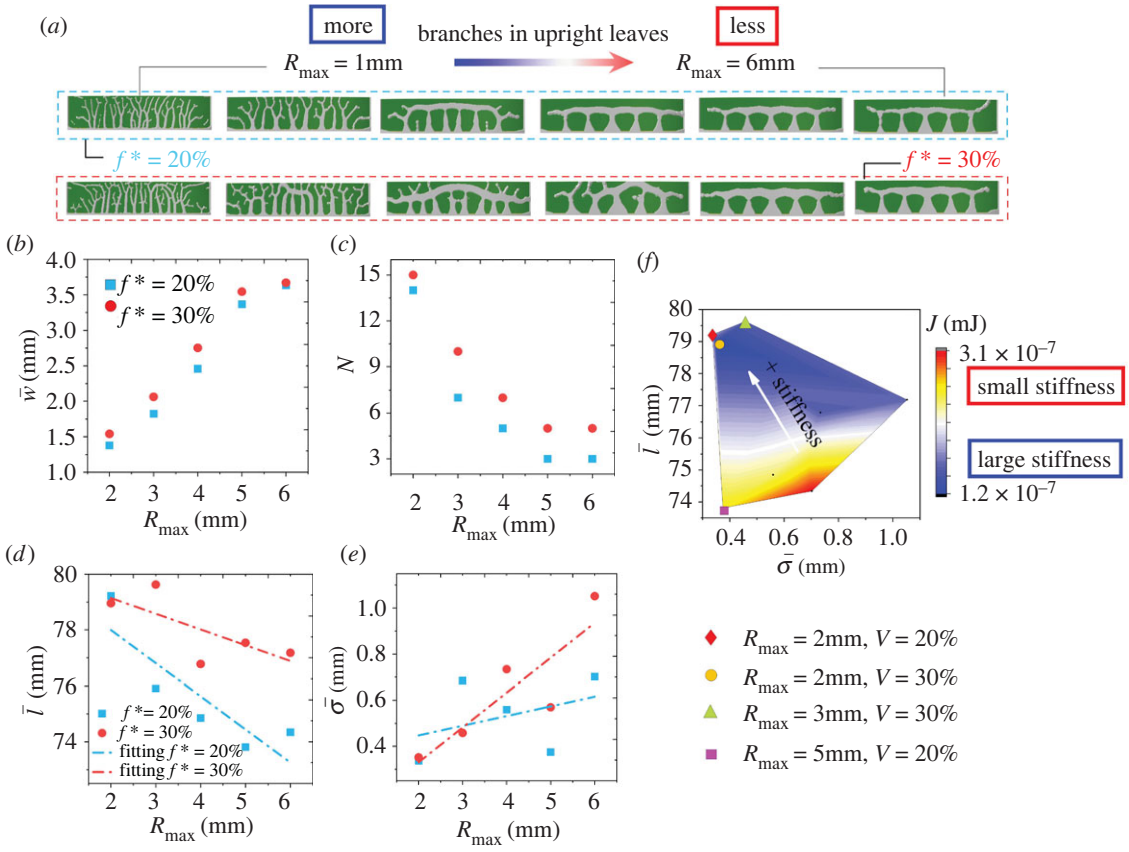

Figure 8. Varying vein features with respect to R_{max}. (*a*) Optimized upright leaves. (*b*) The average wall thickness of the optimized circumferential veins. (*c*) The counted number and (*d*) the maximum layout distance of the circumferential veins. (*e*) The standard error of the wall thickness in circumferential veins. (*f*) The phase diagram of *J* in the $\bar{l}$–$\bar{\sigma}$ space. Three highlighted points are located in the upper-left region, indicating that the vein networks can yield a high stiffness and load-bearing capacity of the leaf.

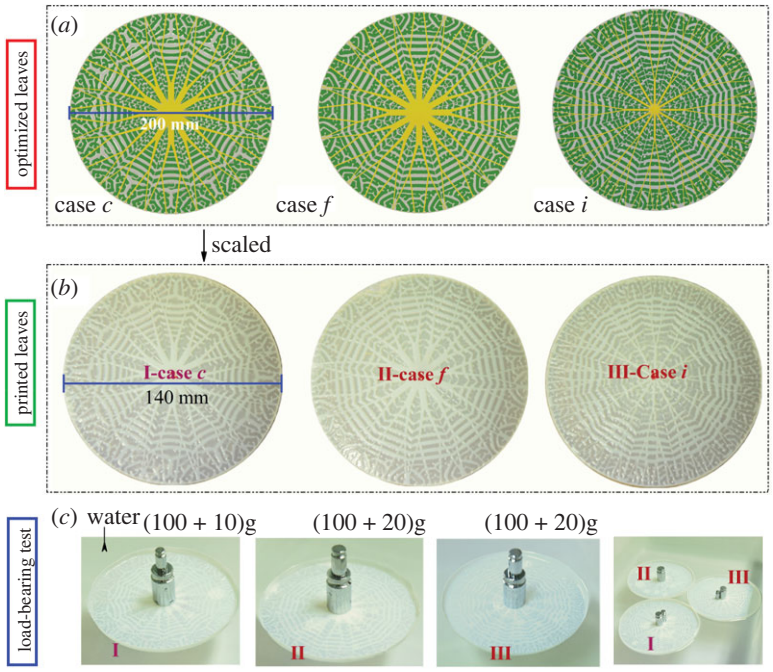

Figure 9. Artificial leaves fabricated by three-dimensional printing technique and their load-bearing capacities. (*a*) Numerical results for the optimized structures of leaves, corresponding to cases *c*, *f* and *i* in figure 5*a*. (*b*) Three-dimensional printed leaves, fabricated according to the numerical optimization results. (*c*) Measurement of the load-bearing capabilities of the artificial leaves. Leaves II (case *f*) and III (case *i*), which are in the second quadrant (figure 6*d*), have better vein topology and higher load-bearing capacity than leaf I (case *c*), which is located in the fourth quadrant.

(material density: 9.2×10^2 kg m^{-3}) and SUP705, respectively. The supporting material SUP705 is dissolved in water and can be easily removed by a high-pressure water jet. The experimental equipment is given in electronic supplementary material, figure S6. We adhere a layer of cling film with glue (electronic supplementary material, figure S7c), which helps improve the quality of the printed samples (electronic supplementary material, figure S7). The weights of glue and film can be ignored.

The optimized results obtained from our numerical simulations using Abaqus are generated and used in the input data of the software Rhino for the three-dimensional printing fabrication. Then three artificial leaf specimens are made, corresponding to the numerical examples described above. As can be seen in figure 9*b*, the printed biomimetic leaves can capture the prominent geometric features of the smaller struts because of the higher printing resolution. The weights of the three samples are 11.6 g, 11.8 g and 11.0 g, respectively. Due to the limitations of the printing condition, all printed leaves are scaled to 0.7 times the initial optimized results (cases *c*, *f* and *i* in figure 9*a*). In addition, the scaled leaves still have an identical stress pattern to the simulation results (figure 4*b*,*c*) because the symmetry in the boundary conditions and loads is not broken.

We use weights to mimic the external loads, which are placed at the centre of the leaf. The loads are 110 g, 120 g and 120 g for the cases *c*, *f* and *i*, respectively. Several tests have been made for each case, and the results are averaged. After removing the supporting material, the printed leaf surface becomes hard several hours later, which endows the leaf with a considerable stiffness. This enhanced surface ensures that the forces generated by the weight can be uniformly distributed to all veins.

According to the weight, the uniform load-bearing pressures are calculated as 1.1 N ($P_1 = 6.5 \times 10^{-5}$ MPa), 1.2 N ($P_1 = 7.8 \times 10^{-5}$ MPa), and 1.2 N (figure 9*c*) for the printed leaves I, II, and III, respectively. As aforementioned in figure 6*d*, leaves II (case *f*) and III (case *i*) are in the second quadrant, in which they have a better vein topology to enhance their load-bearing capacity than that of leaf I located in the fourth quadrant.

5. Conclusion

The. outstanding load-bearing capacity of *Victoria cruziana* leaves results mainly from their peculiar hierarchical vein network structure. A multi-functional optimization method is proposed in this paper to investigate the biomechanical mechanisms in the three-dimensional topological morphology of the veins. The structural optimization of the connected radial and circumferential veins is dictated by the balance of the nutrient transport efficiency and the load-bearing capacity of the leaf. Our simulations show that radial veins with a large branching order *L* not only have a higher efficiency of nutrient delivery, but also are beneficial for the developmental morphologies and layouts of circumferential veins. The load transfer mechanism between the leaf surface and vein is uncovered through the stress pattern analysis. Besides, the experiments of three-dimensional printed artificial leaves also provide a support for our theoretical findings.

Finally, it is noticed that, in the water lily family Nymphaeaceae, apart from *Victoria cruziana* [12–15,17,68,71], the leaf of *Euryale ferox* Salisb. [72–74] also evolves a strong three-dimensional vein network. The multi-functional optimization method proposed in this paper may be extended to understand the possible mechanisms of their morphogenesis by introducing more possible influencing factors. The effects of the intrinsic active mechanisms associated with, for example, cells [2,75], genes [76–78], and biochemical signals on the topological evolution of plant or animal tissues deserve further theoretical and experimental efforts.

Data accessibility. All data needed to evaluate the conclusions in the paper are present in the paper and/or the electronic supplementary material [79]. Electronic supplementary material supporting this article is available online.

The custom codes for modelling and simulation are available from the corresponding author upon reasonable request.

Data have been included in the main paper and electronic supplementary material. The code for the first part of the calculation is available as electronic supplementary material. The second part of the calculation was conducted using Abaqus. This is commercial software which we are unable to share.

Authors' contributions. H.-K.Z.: data curation, investigation, methodology, software, validation, writing—original draft; J.Y.Z.: data curation, investigation, writing—original draft; W.F.: data curation, investigation, writing—original draft; H.C.Z.: funding acquisition, supervision, writing—review and editing; X.D.C.: methodology, writing—original draft; Z.-L.Z.: methodology, writing—review and editing; H.-P.Z.: validation, writing—original draft, writing—review and editing; X.-Q.F.: conceptualization, funding acquisition, methodology, project administration, resources, supervision, writing—review and editing.

All authors gave final approval for publication and agreed to be held accountable for the work performed therein.

Conflict of interest declaration. The authors declare no competing interests.

Funding. Support from the National Natural Science Foundation of China (grant nos. 11921002 and 11872232) is acknowledged.

Acknowledgements. We greatly appreciate the helpful discussion of Dr C. J. Lv and Q. Cui from Tsinghua University and Dr F. Du from the Chinese Academy of Sciences.

References

1. Sapala A *et al.* 2018 Why plants make puzzle cells, and how their shape emerges. *eLife* **7**, e32794. (doi:10.7554/eLife.32794)
2. Thijssen K, Kusters GLA, Doostmohammadi A. 2021 Activity-induced instabilities of brain organoids. *Eur. Phys. J. E* **44**, 147. (doi:10.1140/epje/s10189-021-00149-z)
3. Wang JX, White MD. 2021 Mechanical forces in avian embryo development. *Semin. Cell Dev. Biol.* **120**, 133–146. (doi:10.1016/j.semcdb.2021.06.001)
4. Yang T, Jia ZA, Chen HS, Deng ZF, Liu WK, Chen LN, Li L. 2020 Mechanical design of the highly porous cuttlebone: a bioceramic hard buoyancy tank for cuttlefish. *Proc. Natl Acad. Sci. USA* **117**, 23 450–23 459. (doi:10.1073/pnas.2009531117)
5. Fernandes MC, Aizenberg J, Weaver JC, Bertoldi K. 2021 Mechanically robust lattices inspired by deep-sea glass sponges. *Nat. Mater.* **20**, 237–241. (doi:10.1038/s41563-020-0798-1)
6. Falcucci G, Amati G, Fanelli P. 2021 Extreme flow simulations reveal skeletal adaptations of deep-sea sponges. *Nature* **595**, 537–541. (doi:10.1038/s41586-021-03658-1)
7. Truong H, Engels T, Kolomenskiy D, Schneider K. 2020 Influence of wing flexibility on the aerodynamic performance of a tethered flapping bumblebee. *Theor. Appl. Mech. Lett.* **10**, 382–389. (doi:10.1016/j.taml.2020.01.056)
8. Gao YN *et al.* 2020 Decellularized liver as a translucent ex vivo model for vascular embolization evaluation. *Biomaterials* **240**, 119855. (doi:10.1016/j.biomaterials.2020.119855)
9. Gershlak JR *et al.* 2017 Crossing kingdoms: using decellularized plants as perfusable tissue engineering scaffolds. *Biomaterials* **125**, 13–22. (doi:10.1016/j.biomaterials.2017.02.011)
10. Blonder B, Violle C, Bentley LP, Enquist BJ. 2011 Venation networks and the origin of the leaf

economics spectrum. *J. Exp. Bot.* **14**, 91–100. (doi:10.1111/j.1461-0248.2010.01554.x)

11. Bohn S, Andreotti B, Douady S, Munzinger J, Couder Y. 2002 Constitutive property of the local organization of leaf venation networks. *Phys. Rev. E* **65**, 061914. (doi:10.1103/PhysRevE.65.061914)
12. Hidetoshi K, Yoshimi Y, Kertaro H, Watanabe K. 2009 Vein structue and mechanical propeties of a leaf of santa cruz water lily *Victoria cruziana*. *Jpn. Soc. Mech. Eng.* **21**, 265–266.
13. Lamprecht I, Schmolz E, Hilsberg S, Schlegel S. 2002 A tropical water lily with strong thermogenic behaviour: thermometric and thermographic investigations on *Victoria cruziana*. *Thermochim. Acta* **382**, 199–210. (doi:10.1016/S0040-6031(01)00734-1)
14. Lamprecht I, Schmolz E, Blanco L, Romero CM. 2002 Flower ovens: thermal investigations on heat producing plants. *Thermochim. Acta* **391**, 107–118. (doi:10.1016/S0040-6031(02)00168-5)
15. Junluthin P, Pimpimol T, Whangchai N. 2021 Efficient conversion of night-blooming giant water lily into bioethanol and biogas. *Maejo Int. J. Energy Environ. Commun.* **3**, 38–44.
16. Chang MY, Wu HM, Li HT, Li WJ, Chen SJ, Chen CY. 2014 Secondary metabolites from the leaves of *Victoria amazonica*. *Chem. Nat. Compd.* **50**, 955–956. (doi:10.1007/s10600-014-1131-5)
17. Liu LB, Chen WY. 2013 Structural bionic design for aircraft cover plate based on leaf vein branched structure. *J. Beijing Univ. Aeronaut. Astronaut.* **12**, 1596–1600.
18. Yang PF, Zhang C, Dang F, Yan Y, Liu YL, Chen X. 2016 Abrupt out-of-plane edge folding of a circular thin plate: implication for a mature *Victoria regia* leaf. *Eur. Phys. J. E* **39**, 85. (doi:10.1140/epje/i2016-16085-6)
19. Liu J, Ou HF, He JF, Wen GL. 2019 Topological design of a lightweight sandwich aircraft spoiler. *Materials* **12**, 3225. (doi:10.3390/ma12193225)
20. Liu DC, Hao P, Zhang KP, Tian K, Wang B, Li G, Xu W. 2020 On the integrated design of curvilinearly grid-stiffened panel with non-uniform distribution and variable stiffener profile. *Mater. Des.* **190**, 108556. (doi:10.1016/j.matdes.2020.108556)
21. Wang D, Yeo SY, Su ZC, Wang ZP, Abdalla MM. 2020 Data-driven stream line stiffener path optimization (SSPO) for sparse stiffener layout design of non-uniform curved grid-stiffened composite (NCGC) structure. *Comput. Methods Appl. Mech. Eng.* **365**, 113001. (doi:10.1016/j.cma.2020.113001)
22. Erik AT, Sigmund O, Aage N. 2021 Topology optimization of ultrahigh resolution shell structures. *Thin Wall Struct.* **160**, 107349. (doi:10.1016/j.tws.2020.107349)
23. Feng SQ, Zhang WH, Meng L, Xu Z, Chen L. 2021 Stiffener layout optimization of shell structures with B-spline parameterization method. *Struct. Multidiscip. Optim.* **63**, 2637–2651. (doi:10.1007/s00158-021-02873-8)
24. Wang D, Abdalla MM, Wang ZP, Su ZC. 2019 Streamline stiffener path optimization (SSPO) for embedded stiffener layout design of non-uniform curved grid-stiffened composite (NCGC) structures. *Comput. Methods Appl. Mech. Eng.* **344**, 1021–1050. (doi:10.1016/j.cma.2018.09.013)
25. Fan YC, Dong DY, Li C, Sun YX, Zhang ZY, Wu FL, Yang LW, Li QH, Guan YJ. 2021 Research and experimental verification on topology-optimization design method of space mirror based on additive-manufacturing technology. *Machines* **9**, 354. (doi:10.3390/machines9120354)
26. Zhang WH, Feng SQ. 2022 Combined parameterization of material distribution and surface mesh for stiffener layout optimization of complex surfaces. (https://arxiv.org/abs/2201.09983)
27. Wang C, Zhu JH, Wu MQ, Hou J, Zhou H, Meng L, Li CY, Zhang WH. 2021 Multi-scale design and optimization for solid-lattice hybrid structures and their application to aerospace vehicle components. *Chin. J. Aeronaut.* **34**, 386–398. (doi:10.1016/j.cja.2020.08.015)
28. Ma JM, Zhao ZL, Lin S, Xie YM. 2021 Topology of leaf veins: experimental observation and computational morphogenesis. *J. Mech. Behav. Biomed. Mater.* **123**, 104788. (doi:10.1016/j.jmbbm.2021.104788)
29. Derr NJ, Fronk DC, Weber CA, Mahadevan A, Rycroft CH, Mahadevan L. 2020 Flow-driven branching in a frangible porous medium. *Phys. Rev. Lett.* **125**, 158002. (doi:10.1103/PhysRevLett.125.158002)
30. Lin S, Chen L, Zhang M, Xie YM, Huang XD, Zhou SW. 2020 On the interaction of biological and mechanical factors in leaf vein formation. *Adv. Eng. Softw.* **149**, 102905. (doi:10.1016/j.advengsoft.2020.102905)
31. Sun Z *et al.* 2018 The mechanical principles behind the golden ratio distribution of veins in plant leaves. *Sci. Rep.* **8**, 13859. (doi:10.1038/s41598-018-31763-1)
32. Aage N, Andreassen E, Lazarov BS, Sigmund O. 2017 Giga-voxel computational morphogenesis for structural design. *Nature* **550**, 84–86. (doi:10.1038/nature23911)
33. Bendsøe MP, Sigmund O. 2004 *Topology optimization: theory, methods and applications*. Berlin, Germany: Springer.
34. Bandyopadhyay A, Heer B. 2018 Additive manufacturing of multi-material structures. *Mater. Sci. Eng. R* **129**, 1–16. (doi:10.1016/j.mser.2018.04.001)
35. Guo X, Zhang WS, Zhong WL. 2014 Doing topology optimization explicitly and geometrically: a new moving morphable components based framework. *J. Appl. Mech.* **81**, 081099. (doi:10.1115/1.4027609)
36. Andreassen E, Clausen A, Schevenels M, Lazarov BS, Sigmund O. 2011 Efficient topology optimization in MATLAB using 88 lines of code. *Struct. Multidiscip. Optim.* **43**, 1–16. (doi:10.1007/s00158-010-0594-7)
37. Wang MY, Wang XM, Guo DM. 2003 A level set method for structural topology optimization. *Comput. Methods Appl. Mech. Eng.* **192**, 227–246. (doi:10.1016/S0045-7825(02)00559-5)
38. Tomás Z, Paulino GH. 2015 GRAND3: ground structure based topology optimization for arbitrary 3D domains using MATLAB. *Struct. Multidiscip. Optim.* **52**, 1161–1184. (doi:10.1007/s00158-015-1284-2)
39. Liang Y, Cheng GD. 2019 Topology optimization via sequential integer programming and canonical relaxation algorithm. *Comput. Methods Appl. Mech. Eng.* **348**, 64–96. (doi:10.1016/j.cma.2018.10.050)
40. Svanberg K. 1978 The method of moving asymptotes: a new method for structural optimization. *Int. J. Numer. Methods Eng.* **24**, 359–373. (doi:10.1002/nme.1620240207)
41. Kim YT, Kim YS, Yang C, Park K, Gu GX, Ryu SH. 2021 Deep learning framework for material design space exploration using active transfer learning and data augmentation. *npj Comput. Mater.* **7**, 140. (doi:10.1038/s41524-021-00609-2)
42. Luo YJ, Xing J, Kang Z. 2020 Topology optimization using material-field series expansion and Kriging-based algorithm: an effective non-gradient method. *Comput. Methods Appl. Mech. Eng.* **364**, 112966. (doi:10.1016/j.cma.2020.112966)
43. Gu GX, Chen CT, Buehler MJ. 2018 De novo composite design based on machine learning algorithm. *Extreme Mech. Lett.* **18**, 19–28. (doi:10.1016/j.eml.2017.10.001)
44. Liu JK *et al.* 2018 Current and future trends in topology optimization for additive manufacturing. *Struct. Multidiscip. Optim.* **57**, 2457–2483. (doi:10.1007/s00158-018-1994-3)
45. du Plessis A, Broeckhoven C, Yadroitsava I, Yadroitsev I, Hands CH, Kunju R, Bhate D. 2019 Beautiful and functional: a review of biomimetic design in additive manufacturing. *Addit. Manuf.* **27**, 408–427. (doi:10.1016/j.addma.2019.03.033)
46. Zhang GD, Khandelwal K. 2019 Computational design of finite strain auxetic metamaterials via topology optimization and nonlinear homogenization. *Comput. Methods Appl. Mech. Eng.* **356**, 490–527. (doi:10.1016/j.cma.2019.07.027)
47. Dong HW, Zhao SD, Miao XB, Shen C, Zhang XD, Zhao ZG, Zhang CZ, Wang YS, Cheng L. 2021 Customized broadband pentamode metamaterials by topology optimization. *J. Mech. Phys. Solids* **152**, 104407. (doi:10.1016/j.jmps.2021.104407)
48. Zhang HK, Wu WJ, Kang Z, Feng XQ. 2021 Topology optimization method for the design of bioinspired self-similar hierarchical microstructures. *Comput. Methods Appl. Mech. Eng.* **372**, 113399. (doi:10.1016/j.cma.2020.113399)
49. Zhao Z, Zhang XJS. 2022 Topology optimization of hard-magnetic soft materials. *J. Mech. Phys. Solids* **158**, 104628. (doi:10.1016/j.jmps.2021.104628)
50. Zhao ZL, Zhou SW, Feng XQ, Xie YM. 2018 On the internal architecture of emergent plants. *J. Mech. Phys. Solids* **119**, 224–239. (doi:10.1016/j.jmps.2018.06.014)
51. Liu HX, Hu YM, Zhu B, Matusik W, Sifakis E. 2018 Narrow-band topology optimization on a sparsely populated grid. *ACM Trans. Graph.* **37**, 251. (doi:10.1145/3272127.3275012)

52. Kumar P, Schmidleithner C, Larsen NB, Sigmund O. 2021 Topology optimization and 3D printing of large deformation compliant mechanisms for straining biological tissues. *Struct. Multidiscip. Optim.* **63**, 1351–1366. (doi:10.1007/s00158-020-02764-4)
53. Xu Z, Fan ZC, Pang WB, Zi YY, Zhang YH. 2022 Inverse design strategies for buckling-guided assembly of 3D surfaces based on topology optimization. *Extreme Mech. Lett.* **51**, 101582. (doi:10.1016/j.eml.2021.101582)
54. Forte AE, Hanakata PZ, Jin LS, Zari E, Zareei A, Fernandes MC, Sumner L, Alvarez J, Bertoldi K. 2022 Inverse design of inflatable soft membranes through machine learning. *Adv. Funct. Mater.* **32**, 2111610. (doi:10.1002/adfm.202111610)
55. Tian JW, Li MQ, Han ZH, Chen Y, Gu XFD, Ge QJ, Chen SK. 2022 Conformal topology optimization of multi-material ferromagnetic Soft active structures using an extended level set method. *Comput. Methods Appl. Mech. Eng.* **389**, 114394. (doi:10.1016/j.cma.2021.114394)
56. Zhu JH, Zhang WH, Xia L. 2016 Topology optimization in aircraft and aerospace structures design. *Arch. Comput. Methods Eng.* **23**, 595–622. (doi:10.1007/s11831-015-9151-2)
57. Fernández E, Yang KK, Koppen S, Alarcón P, Bauduin S, Duysinx P. 2020 Imposing minimum and maximum member size, minimum cavity size, and minimum separation distance between solid members in topology optimization. *Comput. Methods Appl. Mech. Eng.* **368**, 113157. (doi:10.1016/j.cma.2020.113157)
58. Wu J, Aage N, Westermann R, Sigmund O. 2018 Infill optimization for additive manufacturing-approaching bone-like porous structures. *IEEE Trans. Vis. Comput. Graph.* **24**, 1127–1140. (doi:10.1109/TVCG.2017.2655523)
59. Bendsoe MP, Sigmund O. 1999 Material interpolation schemes in topology optimization. *Arch. Appl. Mech.* **69**, 635–654. (doi:10.1007/s004190050248)
60. Kumar P, Frouws JS, Langelaar M. 2020 Topology optimization of fluidic pressure-loaded structures and compliant mechanisms using the Darcy method. *Struct. Multidiscip. Optim.* **61**, 1637–1655. (doi:10.1007/s00158-019-02442-0)
61. Bourdin B. 2001 Filters in topology optimization. *Int. J. Numer. Methods Eng.* **50**, 2143–2158. (doi:10.1002/nme.116)
62. Yan XL, Chen JW, Hua HY, Zhang Y, Huang XD. 2021 Smooth topological design of structures with minimum length scale and chamfer/round controls. *Comput. Methods Appl. Mech. Eng.* **383**, 113939. (doi:10.1016/j.cma.2021.113939)
63. Sack L, Scoffoni C. 2013 Leaf venation: structure, function, development, evolution, ecology and applications in the past, present and future. *New Phytol.* **198**, 983–1000. (doi:10.1111/nph.12253)
64. Yan SN, Wang FW, Sigmund O. 2018 On the non-optimality of tree structures for heat conduction. *Int. J. Heat Mass Transfer* **122**, 660–680. (doi:10.1016/j.ijheatmasstransfer.2018.01.114)
65. Zhang XJS, Li WC, Ouyang YF. 2020 Paved guideway topology optimization for pedestrian traffic under Nash equilibrium. *Struct. Multidiscip. Optim.* **63**, 1405–1426. (doi:10.1007/s00158-020-02767-1)
66. Duffly D, Cmok L, Biggins JS. 2021 Shape programming lines of concentrated Gaussian curvature. *J. Appl. Phys.* **129**, 224701. (doi:10.1063/5.0044158)
67. Xu F, Fu CB, Yang YF. 2020 Water affects morphogenesis of growing aquatic plant leaves. *Phys. Rev. Lett.* **124**, 038003. (doi:10.1103/PhysRevLett.124.038003)
68. Tao Y, Wang ZY, Wang K, Feng Q. 2017 Structural bionic design for tower cranes boom based on king lotus leaf vein branched structure. *Mach. Des. Manuf.* **3**, 36–38.
69. Picelli R, Neofytou A, Kim HA. 2019 Topology optimization for design-dependent hydrostatic pressure loading via the level-set method. *Struct. Multidiscip. Optim.* **60**, 1313–1326. (doi:10.1007/s00158-019-02339-y)
70. Hammer VB, Olhoff N. 2000 Topology optimization of continuum structures subjected to pressure loading. *Struct. Multidiscip. Optim.* **19**, 85–92. (doi:10.1007/s001580050088)
71. Lim TK. 2012 *Edible medicinal and non-medicinal plants*, vol. 1. Berlin, Germany: Springer.
72. Khadatkar A, Mehta CR, Gite LP. 2020 Makhana (*Euryle ferox* Salisb.): a high-valued aquatic food crop with emphasis on its agronomic management—a review. *Sci. Hortic.* **261**, 108995. (doi:10.1016/j.scienta.2019.108995)
73. Liu X, He Z, Yin YL, Xu X, Wu WW, Li LJ. 2018 Transcriptome sequencing and analysis during seed growth and development in *Euryale ferox* Salisb. *BMC Genom.* **19**, 343. (doi:10.1186/s12864-018-4707-9)
74. Jana BR, Srivastava A, Idris M. 2018 Climate change effects and quality makhana (*Euryale ferox* Salisb.) production under wetland ecosystem of North Bihar. *Int. J. Curr. Microbiol. Appl. Sci.* **7**, 578–587. (doi:10.20546/ijcmas.2018.712.072)
75. Rozman J, Krajnc M, Ziherl P. 2020 Collective cell mechanics of epithelial shells with organoid-like morphologies. *Nat. Commun.* **11**, 3805. (doi:10.1038/s41467-020-17535-4)
76. Du F, Guan CM, Jiao YL. 2018 Molecular mechanisms of leaf morphogenesis. *Mol. Plant* **11**, 1117–1134. (doi:10.1016/j.molp.2018.06.006)
77. Lu OX, Gao Y, Fu YY, Peng HZ, Shi WJ, Li B, Lv ZY, Feng XQ, Dong B. 2020 Ciona embryonic tail bending is driven by asymmetrical notochord contractility and coordinated by epithelial proliferation. *Development* **147**, dev185868. (doi:10.1242/dev.185868)
78. Azpeitia E *et al.* 2021 Cauliflower fractal forms arise from perturbations of floral gene networks. *Science* **373**, 192–197. (doi:10.1126/science.abg5999)
79. Zhang H-K, Zhou J, Fang W, Zhao H, Zhao Z-L, Chen X, Zhao H-P, Feng X-Q. 2022 Data from: Multi-functional topology optimization of *Victoria cruziana* veins. Figshare. (doi:10.6084/m9.figshare.c.6016902)